High-pressure polymorphs of gadolinium orthovanadate: X-ray diffraction, Raman spectroscopy, and *ab initio* calculations

T. Marqueño,[1,*] D. Errandonea,[1] J. Pellicer-Porres,[1] D. Martinez-Garcia,[1] D. Santamaria-Pérez,[1] A. Muñoz,[2] P. Rodríguez-Hernández,[2] A. Mujica,[2] S. Radescu,[2] S. N. Achary,[3] C. Popescu,[4] and M. Bettinelli[5]

[1]*Departamento de Física Aplicada-ICMUV, Universidad de Valencia, Dr. Moliner 50, Burjassot, 46100 Valencia, Spain*
[2]*Departamento de Física, Instituto de Materiales y Nanotecnología, Universidad de La Laguna, La Laguna 38200, Tenerife, Spain*
[3]*Chemistry Division, Bhabha Atomic Research Centre, Trombay, Mumbai 400 085, India*
[4]*CELLS-ALBA Synchrotron Light Facility, Cerdanyola del Vallès, 08290 Barcelona, Spain*
[5]*Laboratorio Materiali Luminescenti, Dipartimento di Biotecnologie, Università di Verona, and INSTM, UdR Verona, Strada Le Grazie 15, 37134 Verona, Italy*

(Received 3 July 2019; published 28 August 2019)

We present a study of the different high-pressure polymorphs of $GdVO_4$ and its stability. Powder x-ray diffraction and Raman experiments show a phase transition from a zircon- to a scheelite-type structure taking place at 6.8(4) GPa. *Ab initio* density functional theory calculations support this conclusion. The equations of state of these two phases are reported. In addition, we studied the pressure evolution of the Raman modes for the zircon and scheelite phases, showing good agreement between calculations and experiments. For the sake of completeness, we performed optical-absorption measurements up to 16 GPa, showing a band-gap collapse at the transition point. Beyond 20 GPa a second phase transition to a monoclinic fergusonite structure takes place as a consequence of a mechanical instability. A third transition is observed at around 29.3 GPa in Raman experiments. According to our calculations, this fourth polymorph corresponds to an orthorhombic structure described by space group *Cmca*. This phase involves an increase of the atomic coordination number of vanadium and gadolinium. The results are compared to those reported on isomorphic compounds.

DOI: 10.1103/PhysRevB.100.064106

I. INTRODUCTION

Over the last decades, ternary oxides such as tungstates, phosphates, and vanadates have attracted considerable interest due to their outstanding properties, making them suitable for technological purposes. In particular, RVO_4 (R = rare-earth atom) compounds have several important applications, for instance, as laser-host materials, thermophosphors, scintillators, or photocatalytic materials [1–5]. More specifically, rare-earth-doped $GdVO_4$ has been used in solid-state lasers [6–10] and phosphors [11]. Also, the scintillation properties of undoped $GdVO_4$ crystals have been studied, suggesting potential applications in nuclear instrumentation [12].

Apart from $LaVO_4$, rare-earth orthovanadates crystallize in the zircon-type structure [space group (S.G.) $I4_1/amd, Z = 4$] at ambient conditions. Under high pressure (HP), zircon-type orthovanadates with small ionic radii (Nd-Lu) [13] undergo a phase transition to a tetragonal scheelite-type structure (S.G. $I4_1/a$, $Z = 4$), while those with large ionic radii (Ce-Pr) [14] transform into the monoclinic monazite-type structure (S.G. $P2_1/n$, $Z = 8$). $GdVO_4$ belongs to the first group, but its phase diagram is far from being well understood. For instance, Zhang *et al.* [15] performed Raman spectroscopy and luminescence measurements on $GdVO_4$:Eu^{3+} microcrystals up to 16.4 GPa using a methanol-ethanol mixture as pressure transmitting medium (PTM), showing a zircon-scheelite phase transition at 7.4 GPa. In another study carried out by Huang *et al.* [16], metastable scheelite-type RVO_4 samples (including $GdVO_4$) were analyzed at ambient pressure by means of x-ray diffraction (XRD) and Raman spectroscopy. Since the frequencies of the Raman modes found in Ref. [16] show some discrepancies with those reported in Ref. [15], we expect that our results will shed light on the vibrational behavior of the gadolinium orthovanadate. Moreover, Hong *et al.* [17] reported HP XRD and photoluminescence measurements on $GdVO_4$:Er^{3+} using silicone oil as PTM. They found two phase transitions at 7.4 (zircon to scheelite) and 23.1 GPa (scheelite to fergusonite). By contrast, XRD experiments have been carried out on undoped $GdVO_4$ under nonhydrostatic conditions which show the onset of the zircon-scheelite and scheelite-fergusonite transitions at 5.0 and 31.2 GPa, respectively [18]. It is known that differences in the experimental conditions, such as the degree of hydrostaticity [19] and sample purity, can affect either the transition pressure [20] or the phase sequence [13,14,21–23]. Therefore, a systematic study is needed in order to accurately understand structural the behavior of $GdVO_4$ under compression.

With the aim of providing a better understanding of its structural properties and searching for additional phase transitions, we have investigated the evolution of $GdVO_4$ under HP conditions by performing XRD and Raman spectroscopy experiments up to 26 and 39 GPa, respectively. Furthermore, we carried out *ab initio* calculations up to 31 GPa in order to analyze the mechanical and dynamical stability of the different phases. The polymorphs relevant for our study are shown

*tomas.marqueno@uv.es

 ©2019 American Physical Society

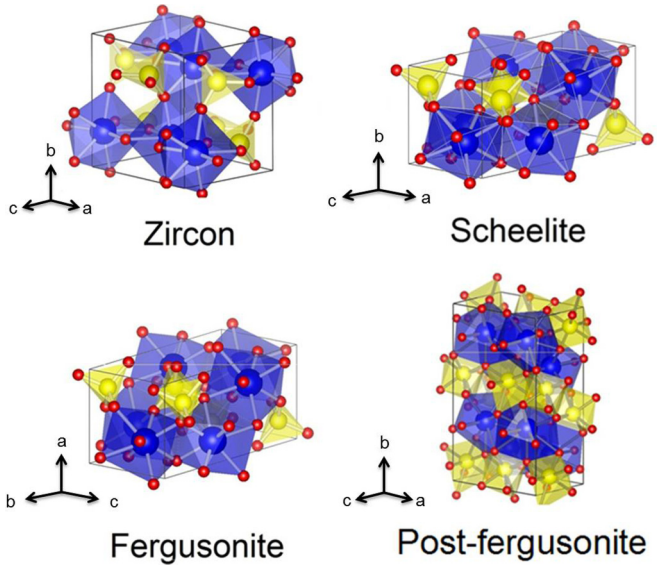

FIG. 1. Unit cells of the different high-pressure polymorphs of $GdVO_4$. The blue, yellow, and red spheres stand for the Gd, V, and O atoms. Polyhedral units of Gd and V are also shown.

in Fig. 1. The agreement between theory and experiments has allowed us to assess the evolution of the atomic positions as well as the phonon frequencies under HP. In addition, accurate room temperature equations of state (EOS) and axial compressibilities of zircon- and scheelite-type $GdVO_4$ are reported. Additionally, we carried out optical-absorption measurements on $GdVO_4$ single crystal up to 16 GPa. As a result, we obtained the evolution of the band gap of the zircon and scheelite phases.

II. METHODS

A. Experimental details

Polycrystalline $GdVO_4$ used in Raman and x-ray diffraction experiments were prepared by solid-state reaction of appropriate amounts of predried Gd_2O_3 and V_2O_5 (99.9% purity). A homogeneous mixture of the oxides was pelletized and heated at 800 °C for 24 h and subsequently cooled to ambient temperature. The product was reground and heated at 1100 °C for 24 h. $GdVO_4$ single crystals used in the optical-absorption experiments were prepared by the flux growth method using $Pb_2V_2O_7$ as solvent [24]. As starting materials, we used appropriate quantities of pure V_2O_5, PbO, $Na_2B_4O_7$, and 99.99% purity Gd_2O_3. The starting mixture was sealed in a Pt crucible and heated to 1270 °C in a horizontal furnace. The melt was kept at 1270 °C for 12 h and then slowly cooled to 800 °C. The crucible was then removed and quickly inverted to separate the flux from the crystals. Transparent crystals with average size $3 \times 2 \times 1\,mm^3$ were separated from the flux by dissolving it in hot diluted HNO_3. XRD at ambient conditions confirmed the zircon-type phase both in polycrystalline and single-crystal samples with similar lattice parameters, $a = 7.198(6)$ Å and $c = 6.353(3)$ Å, which agrees with those previously reported [25]. These measurements did not detect the presence of impurities, secondary phases, or the starting materials used to prepare $GdVO_4$, suggesting that our samples were of high purity.

The HP angle-dispersive x-ray diffraction (ADXRD) experiment was performed using a diamond-anvil cell (DAC) with diamond culets of 350 μm diameter. The sample was loaded in a 150-μm-diameter hole drilled on an Inconel gasket preindented to 40 μm thickness. Finely ground powdered $GdVO_4$ was loaded together with Cu grains. The EOS of Cu was used as a pressure scale [26]. Ar was employed as PTM to guarantee quasihydrostatic conditions for $P < 20$ GPa [27]. Ar peaks were used to confirm the pressure determined from Cu [28]. Special care was taken when loading the DAC to avoid sample bridging between the diamond anvils [29,30]. The experiment was performed at the MSPD beamline of the ALBA-CELLS synchrotron [31] using a monochromatic x-ray beam ($\lambda = 0.4246$ Å) focused down to $20 \times 20\,\mu$m (FWHM). XRD data was collected using a Rayonix CCD detector located 240 mm from the sample. A rocking angle of $\pm 3°$ was used to improve the homogeneity of the Debye rings. The images collected in the CCD were transformed to intensity vs 2θ patterns with the program DIOPTAS [32]. Structural analyses were performed with the POWDERCELL [33] and FULLPROF [34] software packages. Since the XRD patterns collected under HP were affected by preferred orientation effects [35], we did not perform Rietveld refinements but a LeBail analysis [36], determining only the unit-cell parameters of the different structures. Notice that this does not preclude the unambiguous identification of the crystal structures of the reported phases.

Raman measurements were carried out in a setup built with a confocal microscope, an edge filter, a 1-m focal-length spectrometer equipped with a 600 grooves/mm grating (TRH 1000, JobinYvon), and a thermoelectric-cooled multichannel CCD detector. The spectral resolution is better than $2\,cm^{-1}$. Wave numbers were calibrated using the laser plasma lines. Raman spectra were obtained using a He-Ne laser ($\lambda = 632.8$ nm) with an incident power of 10 mW on the sample. At HP, two independent experiments were performed with the same DAC employed in XRD experiments. We used steel and rhenium gaskets in the first and the second experiment, respectively. Both gaskets were preindented to a 40 μm thickness and had a 200-μm-diameter hole. In this case, Ne was the PTM, and pressure was determined using the ruby fluorescence method [37].

In optical-absorption measurements we studied small single crystals of size $\sim 80 \times 80\,\mu$m and thickness $\sim 10\,\mu$m. The samples were loaded in a 200-μm-diameter hole of an Inconel gasket preindented to 50 μm in a DAC equipped with IIA-type diamond anvils with a culet size of 480 μm. In this case, the PTM was a mixture of ethanol-methanol-water (16:3:1). The pressure was measured using the ruby luminescence method [37]. The maximum pressure achieved was 16 GPa. The optical-absorption measurements were carried out using an optical setup consisting of a deuterium lamp, fused silica lenses, reflecting optics objectives, and an UV-visible near-infrared spectrometer.

B. Simulation details

Computer simulations for $GdVO_4$ were performed with the Vienna Ab Initio Simulation Package (VASP) [38,39], within the framework of the density functional theory

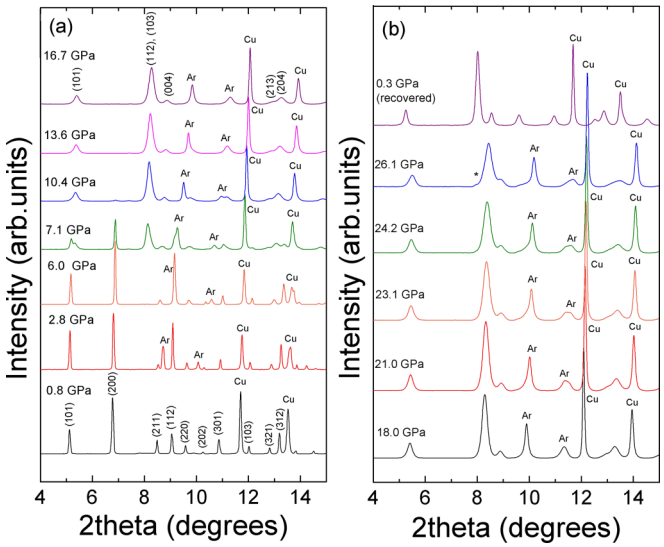

FIG. 2. Selected powder XRD patterns (a) from 0.8 to 16.7 GPa and (b) from 19.4 to 26.1 GPa. The figure (b) also includes an XRD pattern of the recovered sample. Some selected reflections of the zircon- and scheelite-type phases are indicated at 0.8 and 16.7 GPa, respectively. Ar and Cu peaks are indicated. The asterisks identify the most intense reflection associated with V_2O_5.

(DFT) [40]. The pseudopotential method and the projector augmented wave scheme (PAW) [41] were employed, and the exchange-correlation energy was described using the generalized-gradient approximation (GGA) with the Perdew-Burke-Ernzerhof (PBE) [42] prescription. The highly localized nature of the $4f$ electrons of Gd was described by Dudarev's GGA + U method [43], with an effective U value of 3.4 eV [44]. To guarantee highly converged results, we used a basis of plane waves up to a kinetic energy cutoff of 520 eV and a dense Monkhorst-Pack k-special points grid to perform the integrations on the Brillouin zone (BZ). In a set of selected volumes, the structural configurations were completely optimized by minimizing the forces on the atoms and the stress tensor. Our optimization criteria were to achieve forces smaller than 0.006 eV/Å and differences among the diagonal components of the stress tensor lower than 0.1 GPa. The phonon calculations were performed at the zone center (Γ point) of the BZ with the small-displacement method, which has been shown to work properly for studying phonons under compression [45,46].

III. RESULTS AND DISCUSSION

A. XRD experiments

In Fig. 2(a) selected powder XRD patterns are displayed from 0.8 to 16.7 GPa. A few peaks do not belong to the sample but to the PTM and the pressure standard, labeled as "Ar" and "Cu." The diffraction peaks of the sample from ambient pressure up to 6.0 GPa can be undoubtedly identified as a zircon-type structure. The unit-cell parameters determined at 0.8 GPa are $a = 7.186(4)$ Å and $c = 6.341(3)$ Å (S.G. $I4_1/amd$, $Z = 4$). These values are consistent with those reported at ambient pressure [25,47–49]. When pressure reaches 7.1 GPa, extra diffraction peaks appear, which can be assigned to the scheelite structure. Beyond this pressure, there is a zircon-scheelite phase coexistence up to 10.4 GPa. The zircon peaks gradually disappear, and the scheelite phase finally appears as a single phase at 11.6 GPa. For $P > 8$ GPa only the zircon (200) reflection can be seen, so the unit-cell parameters of this structure cannot be determined. At 13.6 GPa, the unit-cell parameters of the scheelite structure are $a = 4.963(4)$ Å and $c = 11.023(5)$ Å (S.G. $I4_1/a$, $Z = 4$). As it is shown in Fig. 2(a), the scheelite peaks are considerably broader than the zircon peaks. This could be explained by a strain increase and a grain size reduction produced as a consequence of the large volume collapse associated with this transition ($\Delta V/V_0 = 10.8\%$). In fact, after carrying out a Williamson-Hall analysis [50] we obtain a strain parameter $\xi_Z = 3.3 \times 10^{-3}$ and a mean linear grain size of $t_Z \sim 330$ nm for the zircon phase at 5.2 GPa, whereas for the scheelite we obtain $\xi_S = 8.2 \times 10^{-3}$ and $t_S \sim 60$ nm at 13.2 GPa. The loss of crystallinity associated with this transition was also reported for $ErVO_4$ [51].

Above 20 GPa, the scheelite peaks start to broaden upon compression [see Fig. 2(b)]. This can be explained as a consequence of a mechanical instability of the scheelite phase that *ab initio* calculations predict to occur at 22.8 GPa (see below). The deterioration of the hydrostatic conditions [27] could contribute to reduce the transition pressure. Actually, the evolution of the peaks beyond 20 GPa is incompatible with the scheelite structure, and they are better described by a monoclinic distortion of it. This suggests that a scheelite-to-fergusonite ($I2/a$, $Z = 4$) phase transition takes place, which has been observed at similar pressures in other rare-earth orthovanadates [13,20,52–54]. Under nonhydrostatic conditions (no PTM), this phase transition has been reported to take place above 31.2 GPa in $GdVO_4$ [18]. In our experiment, at 26 GPa, an additional weak peak appears at $2\theta \sim 8°$, which is indicated in Fig. 2(b) with an asterisk. This reflection (which was not observed in the starting samples and at lower pressure) cannot be explained with a fergusonite structure, but it can be assigned to the most intense peak of V_2O_5 [55]. A possible scenario may be a partial x-ray-induced dissociation of V_2O_5 units, which has been observed in other XRD experiments on rare-earth orthovanadates [13,50]. Similar findings have been reported for ternary oxides as a consequence of the photoelectric processes triggered by the x ray's interaction with the sample [56]. Upon decompression, the scheelite structure is recovered at 21.0 GPa. A metastable scheelite phase was quenched to 0.3 GPa, as it is shown in Fig. 2(b). Therefore, the second phase transition is reversible (scheelite-fergusonite) whereas the first phase transition (zircon-scheelite) is irreversible. Many other zircon-structured materials have shown the same trend, including related vanadates [13,51–54,57,58].

Figure 3 shows the pressure dependence of the lattice parameters. In this figure our theoretical and experimental data and the results reported by Yue *et al.* [18] are compared. The deviation between experimental and theoretical sets of data is small. Our experimental results (using Ar as PTM) are much less dispersed and in much better agreement with *ab initio* calculations than those obtained under nonhydrostatic conditions. Yue *et al.* [18] reported the onset of the phase transition at 5.0 GPa, while we found the transition at 6.6(5) GPa. Nonhydrostaticity has also been associated in

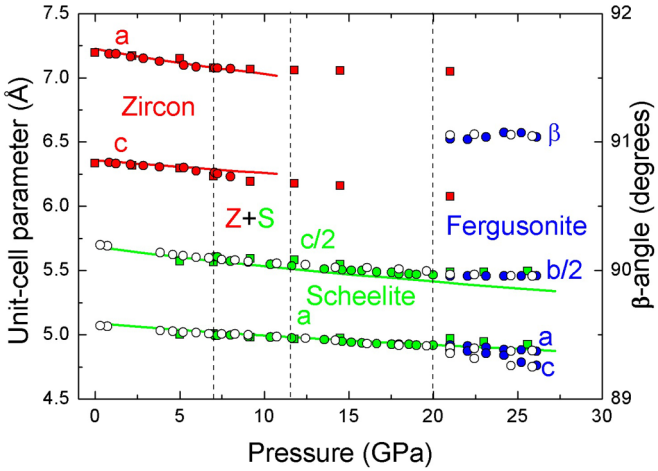

FIG. 3. Pressure evolution of the unit-cell parameters. The different phases are indicated in colors within the figure. Circles stand for our data and squares represent the data reported by Yue and co-workers [18]. Solid and empty symbols denote experimental data obtained upon compression and decompression, respectively. Theoretical calculations are represented by solid lines. Dashed vertical lines tentatively indicate the different phases and phase coexistences.

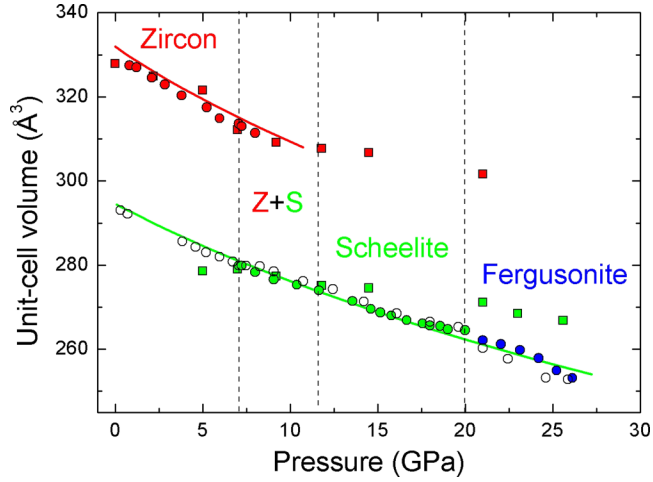

FIG. 4. Unit-cell volume vs pressure. The meaning of the symbols is the same as that indicated in Fig. 3.

other RVO_4 compounds to a reduction of the phase transition pressure. As an example, in $HoVO_4$ nonhydrostaticity reduces the transition pressure from 8.2 to 4 GPa [20]. Zhang *et al.* [15] and Hong *et al.* [17] found the onset of the phase transition below 7.4 GPa in $GdVO_4$:Eu^{3+} and $GdVO_4$:Er^{3+}, respectively, which is compatible with our results.

The axial compressibilities of zircon-type $GdVO_4$ can be estimated by a linear function. As a result, we obtain $\kappa_a = 2.6 \times 10^{-3}$ and $\kappa_c = 1.9 \times 10^{-3}$ GPa^{-1} from our experiments, which are similar to the theoretical axial compressibilities $\kappa_a = 2.7 \times 10^{-3}$ and $\kappa_c = 1.6 \times 10^{-3}$ GPa^{-1}. In both cases, the a axis is more compressible than the c axis. This fact can be explained in terms of different compressibilities of GdO_8 and VO_4 polyhedral units and their disposition within the zircon structure. The structure can be described as a chain of alternating edge-sharing GdO_8 dodecahedra and VO_4 tetrahedra along the c-axis and edge-sharing GdO_8 dodecahedra in the a-axis direction, and, as we will see further on, the GdO_8 units are more compressible than the VO_4 tetrahedra. Once the fergusonite-to-scheelite phase transition is achieved at 21.0 GPa, the monoclinic β angle suddenly increases up to $\sim 91^\circ$ and remains approximately constant between 21 and 26 GPa. As expected, the a and c axes of the fergusonite structure diverge, corresponding both to the a axis of the scheelite phase, and there is no discontinuity between the scheelite c axis and the fergusonite b axis. These changes are compatible with a second-order displacive transition.

In Fig. 4 we show the pressure dependence of the unit-cell volumes of the zircon, scheelite, and fergusonite phases of $GdVO_4$. For the first two phases, they are fitted to a third-order Birch-Murnaghan equation of state (BM EOS) [59] to obtain the ambient pressure bulk moduli K_0, their first derivative K_0', and the ambient pressure unit-cell volumes V_0. The P-V results of the fergusonite phase are not analyzed because of insufficient data. The obtained parameters for both zircon and scheelite phases are given in Table I together with the results of our calculations and values reported in literature. Our experimental values for zircon and scheelite-type $GdVO_4$ are very similar to the values found for Er-doped $GdVO_4$ (10% Er) [17]. In addition, the zircon phase has a bulk modulus 11% smaller than the scheelite phase, which is coherent with the 10.8% volume collapse and the increase of the packing efficiency of the second phase. The agreement between the theory and the experiments is considerably good for the ambient pressure unit-cell volume and the bulk modulus. On the other hand, under nonhydrostatic conditions (no PTM) the structure seems to be much less compressible, especially for the scheelite phase. Thus, the presence of deviatoric stresses may cause an increase of the bulk modulus value. Only in the case of zircon-type $GdVO_4$:Er^{+3} [17] in which silicon oil was used as PTM, the bulk modulus is lower than the one obtained under quasihydrostatic conditions. However, this does not constitute a strong discrepancy from the general trend since the associated error bar is considerable. The influence of the PTM has been analyzed in many other vanadates, showing a reduction of the bulk compressibility as nonhydrostaticity increases [20,52,60,61].

As mentioned above, the zircon structure can be described as chains of alternating edge-sharing VO_4 tetrahedra and

TABLE I. EOS parameters for the zircon and scheelite phases of $GdVO_4$.

Phase	Conditions	V_0 (Å^3)	K_0 (GPa)	K_0'
Zircon (this work)	Theory	331.9	117.3	5.5
Zircon (this work)	Ar	330.0(5)	122(5)	4.2(1.5)
Zircon [16]	Silicon oil	327(2)	102(14)	4 (fixed)
Zircon [17]	None	327(2)	185(28)	4 (fixed)
Scheelite (this work)	Theory	294.5	138.03	3.9
Scheelite (this work)	Ar	293.4(6)	137(2)	6(2)
Scheelite [16]	Silicon oil	289.6(1.4)	137(15)	4 (fixed)
Scheelite [17]	None	283.6(9)	379(32)	4.0
Postfergusonite (this work)	Theory	535.9	110.7	4.5

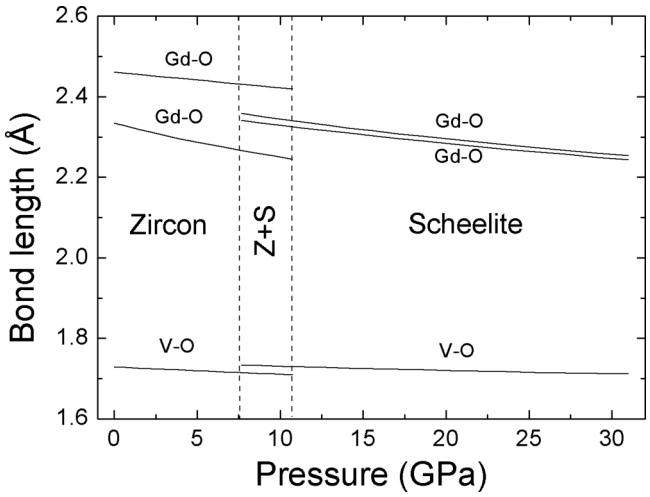

FIG. 5. Theoretical evolution of the Gd-O and V-O bond lengths with pressure in zircon- and scheelite-type $GdVO_4$.

GdO_8 dodecahedra extending along the *c*-axis direction and edge-sharing GdO_8 dodecahedra along the *a* axis. After the transition, the scheelite phase emerges and the polyhedra within the unit-cell change its relative positions and orientations so that the VO_4 tetrahedra are no longer edge shared. Our calculations provide the pressure dependence of the interatomic bond distances, which is shown in Fig. 5. For both zircon and scheelite phases, the GdO_8 units are not regular but slightly distorted since there are two different Gd-O distances. After the zircon-to-scheelite phase transition, the two Gd-O distances and their compressibilities become more similar and the bond-length distortion of the dodecahedra is reduced by an order of magnitude. In particular, the bond-length distortion indices of the GdO_8 units for the zircon and scheelite phases are ∼0.03 and ∼0.003, respectively. The evolution of the interatomic distances is coherent with some previous reported data on other RVO_4 compounds [20,62]. Since the Gd-O bonds are more compressible, the GdO_8 dodecahedron is mainly responsible for most of the pressure-induced volume change. Just after the transition, there is an ∼4% volume increase of the VO_4 tetrahedra, while the volume of the GdO_8 dodecahedra stays about the same. This is not in contradiction with the huge volume collapse observed since this is caused by the reordering of the VO_4 tetrahedra. Similar behavior has been reported for many other zircon and scheelite-type molybdates [63] and phosphates [64].

B. Raman scattering experiments

Zircon-type compounds have twelve Raman-active modes ($\Gamma_R = 2A_{1g} + 4B_{1g} + B_{2g} + 5E_g$) [65]. Figure 6(a) shows representative Raman spectra of zircon-type $GdVO_4$ at different pressures. Only 9 out of 12 modes are observed; their symmetry has been assigned in accordance with our calculations and the literature [66]. As in other isomorphic compounds, there is a large frequency gap between 500 and 800 cm^{-1} so the spectra can be divided into two regions of low and high frequencies. The modes in the high-frequency region can be considered in good approximation as internal vibrations of the VO_4 tetrahedron [67]. In order to facilitate the discussion, different modes with the same symmetry will be identified with a different supra-index along the article. At 1.2 GPa, the internal symmetric-stretching mode $A_g^{(1)}$ at 893 cm^{-1} clearly dominates the Raman spectrum of zircon-type $GdVO_4$, together with the $E_g^{(1)}$ and $B_g^{(1)}$ asymmetric-stretching modes at 824 and 818 cm^{-1}, respectively. Regarding the low-frequency region, it can be seen that the peak which corresponds to the $A_{1g}^{(2)}$ vibration has an asymmetric profile. Polarization studies using different scattering geometries have shown that this line

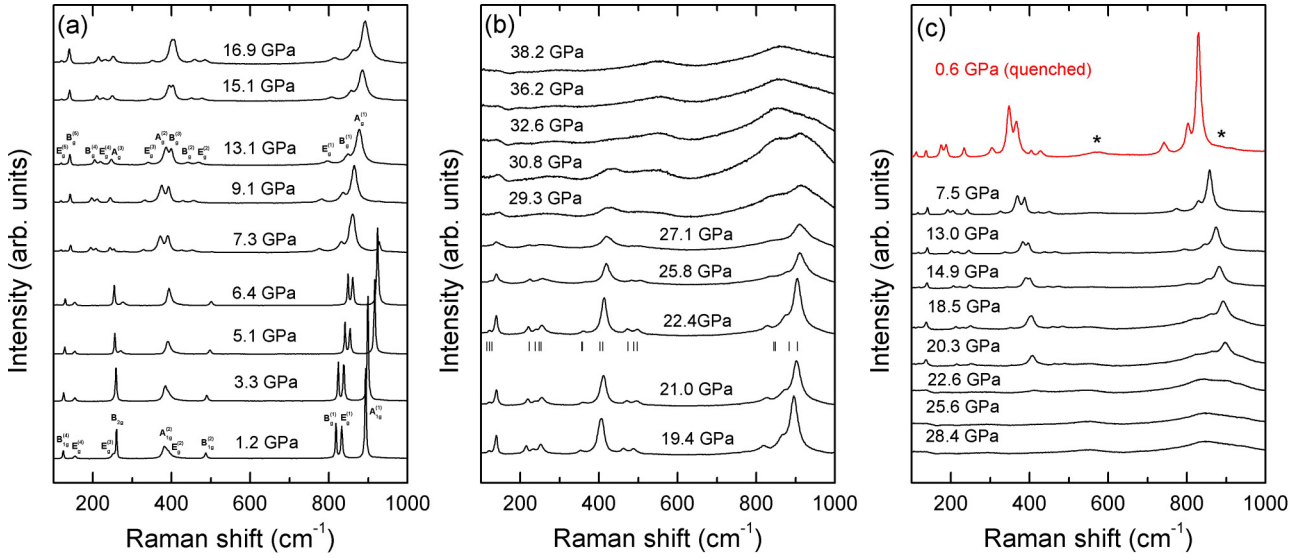

FIG. 6. Raman spectra of $GdVO_4$ (a) from 1.2 to 16.9 GPa and (b) from 19.4 to 38.2 GPa. (c) The Raman spectra obtained on pressure release. The spectra shown in (a) were obtained in the first run using a steel gasket while those shown in (b) and (c) were obtained in the second run using a rhenium gasket. The black ticks on (b) stand for the calculated Raman modes for the fergusonite phase obtained at 22.4 GPa in the XRD experiments (structural parameters are shown in Table IV). The spectrum of the recovered sample is displayed in red color in (c). Asterisks denote the bands associated with the postfergusonite phase.

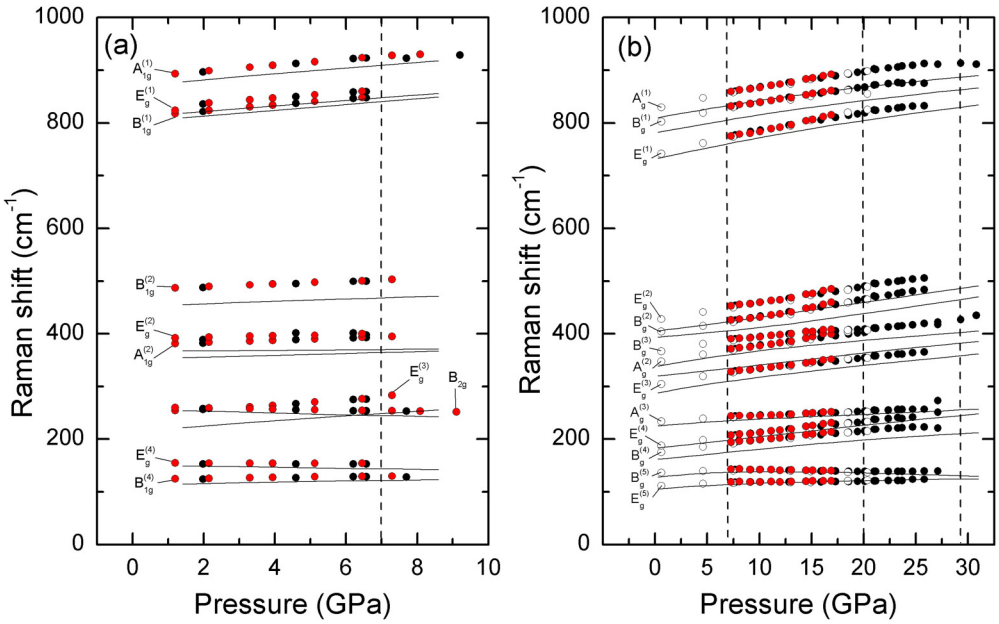

FIG. 7. Evolution of the Raman frequency of the modes in (a) zircon- and in (b) scheelite-type $GdVO_4$. Red circles represent the data collected in run 1, whereas black and empty symbols stand for the data obtained in run 2 upon compression and decompression, respectively. The theoretical modes are represented by solid black lines. In (b), beyond 20 GPa we are representing the evolution of the peaks observed in the spectra, which, for at least some of them, could not be single, since this phase is associated with a fergusonite phase.

consists of two different modes [66]. They have been proposed to be the $A_{1g}^{(2)}$ and $E_g^{(2)}$ modes [68]. Our calculations predict a very small difference between these two modes (352 and 366 cm^{-1}, respectively). Therefore, it can be assumed that the above-described peak asymmetry is produced by the proximity in frequency of these two Raman modes. Considering this, the modes $B_{1g}^{(2)}$, $E_g^{(2)}$, $A_{1g}^{(2)}$, and B_{2g} are found at 486, 392, 382, and 260 cm^{-1}, respectively ($P = 1.2$ GPa). The $B_{1g}^{(3)}$ and $E_g^{(5)}$ modes are not observed in our spectra due to their weak Raman scattering cross section. These peaks are visible only using $GdVO_4$ single crystals (when measured outside the DCA) in certain scattering geometries [66].

The evolution of the zircon-type structure vibrational modes with pressure is displayed in Fig. 7(a). It is noticeable that, despite the fact that calculations underestimate the frequency of the modes (from 1% to 13% lower), the predicted behavior of these modes upon compression seems to reasonably agree with the experiments. As shown, most modes depend linearly on pressure and only the low-frequency modes $E_g^{(4)}$ and B_{2g} exhibit a weak soft-mode behavior. The values of the pressure coefficients ($d\omega/dP$), the estimated zero-pressure frequency, and the corresponding Grüneisen parameters are displayed in Table II, showing a reasonable good agreement between theory and experiments. The Grüneisen parameters were calculated taking the bulk modulus $K_0 =$ 122 GPa. The high-frequency $A_g^{(1)}$, $E_g^{(1)}$, and $B_g^{(1)}$ modes and the low-frequency $E_g^{(3)}$ mode have a stronger dependency on pressure than the rest of the modes. As a consequence of the large positive pressure coefficient of the $E_g^{(3)}$ mode and the softening of the B_{2g} mode, there is a crossover of these two modes at ~3 GPa. This mode crossover has been observed in other different vanadates [51,55,69–71] as well as in doped $GdVO_4$ [15]. Among the low-frequency modes, the $E_g^{(3)}$ mode shows the strongest dependence on pressure, which is also a common behavior in vanadates [51,55,67–69]. In Table II we also included the data reported by Zhang *et al.* [15] and Voron'ko *et al.* [66] for the sake of comparison. The agreement of the data reported by Zhang *et al.* [15] and ours is reasonably good except for the $E_g^{(4)}$ mode. Our calculations and experiments show that this mode softens (negative pressure coefficient), whereas Zhang *et al.* [15] report a positive linear dependence with pressure. The origin of this discrepancy may be the fact that the value of $d\omega/dP$ is very close to zero and thus it is comparable to the dispersion of the data. Therefore, even though the sign is the opposite, the discrepancy is comparable to the margin of error.

From our observations we can infer that the zircon-to-scheelite transitions take place between 6.4 and 7.3 GPa. Therefore, since the scheelite phase appears between 6.0 and 7.1 GPa in our XRD experiments, a more accurate value of the transition pressure would be 6.8(4) GPa. The Raman spectra showing the progressive zircon-to-scheelite transitions are displayed in Fig. 6(a). According to group theory, the scheelite structure has thirteen Raman-active modes ($\Gamma_R = 3A_g + 5B_g + 5E_g$) [72,73]. In our experiment, all the scheelite modes are visible. As in the zircon phase, the spectra of the scheelite phase show a frequency gap (~550−750 cm^{-1}) that divides them into the low- and high-frequency regions. The assignment of the modes was made in accordance with literature [74]. After the onset of the transition, there is a coexistence of both phases up to 9.1 GPa. Above this pressure the scheelite structure appears as a single phase. As in the case of the zircon structure, the Raman spectrum is dominated by the symmetric-stretching $A_g^{(1)}$ mode, located at 877 cm^{-1} at 13 GPa. Also, the frequency of this mode is the highest one. The asymmetric-stretching modes $B_g^{(1)}$ and the $E_g^{(1)}$ are located at 848 and 796 cm^{-1}, respectively. In the low-frequency

TABLE II. Theoretical and experimental zero-pressure frequencies, pressure coefficients, and Grüneisen parameters of the Raman modes in zircon-type $GdVO_4$. Our results are also compared to the data obtained by Zhang *et al.* [15] and Voron'ko *et al.* [66] for zircon-type $GdVO_4$.

	Theory			Experiment			Zhang *et al.* [15]		Voron'ko *et al.* [66]
Mode	$d\omega/dP$ (cm^{-1}/GPa)	ω_0 (cm^{-1})	γ	$d\omega/dP$ (cm^{-1}/GPa)	ω_0 (cm^{-1})	γ	$d\omega/dP$ (cm^{-1}/GPa)	ω_0 (cm^{-1})	ω_0 (cm^{-1})
$E_g^{(5)}$	1.46	105.3	1.62	–	–	–	–	–	110
$B_{1g}^{(4)}$	1.59	112.8	1.65	1.19(8)	123	1.18(9)	0.9	124	123
$E_g^{(4)}$	−0.96	150.5	−0.75	−0.21(5)	155	−0.17(4)	0.1	156	156
$E_g^{(3)}$	4.86	214.7	2.66	4.7(3)	247	2.32(18)	4.5	245	246
$B_{1g}^{(3)}$	2.66	237.4	1.31	–	–	–	–	–	252
B_{2g}	−1.62	256.4	−0.74	−1.02(2)	261	−0.48(2)	−0.8	263	261
$A_{1g}^{(2)}$	1.75	352.3	0.58	2.16(4)	379	0.72(6)	1.7	384	380
$E_g^{(2)}$	0.51	366.5	0.16	1.4(1)	391	0.49(7)	–	–	438
$B_{1g}^{(2)}$	2.37	451.6	0.62	2.60(4)	484	0.66(3)	2.5	485	483
$B_{1g}^{(1)}$	5.58	801.6	0.82	5.78(2)	811	0.87(4)	5.2	811	809
$E_g^{(1)}$	5.25	811.2	0.76	5.24(2)	827	0.77(3)	5.31	827	825
$A_{1g}^{(1)}$	5.67	870.0	0.76	5.51(14)	887	0.76(4)	5.5	887	884

region, we observed the $E_g^{(5)}$ mode at 119 cm^{-1} ($P = 13$ GPa), which was not reported before. Figure 7(b) shows the pressure dependence of both calculated and experimental scheelite modes. All of the different modes, except for $B_g^{(5)}$, show a definite positive linear dependence on pressure. Their pressure coefficients, zero-pressure frequencies, and Grüneisen parameters (calculated by taking $K_0 = 137$ GPa) are summarized in Table III. The data obtained by Zhang *et al.* [15] and Huang *et al.* [16] are included in this table for the sake of comparison. In general, the agreement with the data reported by Zhang *et al.* [15] is reasonably good except for the pressure coefficients of the $E_g^{(2)}$ and $B_g^{(1)}$ modes, which seem to be underestimated in their work. Also, the $B_g^{(4)}$ mode peak is mislabeled in Ref. [15], since they identified it as an E_g mode (this is indicated with an asterisk in Table III). The frequency of the $E_g^{(5)}$, $B_g^{(5)}$, and $B_g^{(4)}$ modes reported by Huang *et al.* [16] at ambient pressure does not match with ours or those reported by Zhang *et al.* [15]. The origin of this discrepancy may be the presence of some impurities or/and a minor quantity of zircon-type $GdVO_4$ in the synthesized sample obtained by Huang *et al.* [16].

Another interesting feature is that the Raman spectra reported in Ref. [15] show an unexplained peak at ∼900 cm^{-1} that appears when the zircon-to-scheelite phase transition takes place. We think that the presence of this peak can be attributed to the presence of V_2O_5 [75], probably caused

TABLE III. Calculated and empirical zero-pressure frequencies, pressure coefficients, and Grüneisen parameters of the Raman modes in scheelite-type $GdVO_4$. We include the data obtained by Zhang *et al.* [15] and Huang *et al.* [16] for the sake of comparison. The values indicated with an asterisk are labeled as $T(E_g)$ in Zhang *et al.* [15].

	Theory			Experiment			Zhang *et al.* [15]		Huang *et al.* [16]
Mode	$d\omega/dP$ (cm^{-1}/GPa)	ω_0 (cm^{-1})	γ	$d\omega/dP$ (cm^{-1}/GPa)	ω_0 (cm^{-1})	γ	$d\omega/dP$ (cm^{-1}/GPa)	ω_0 (cm^{-1})	ω_0 (cm^{-1})
$E_g^{(5)}$	0.76	109.5	1.05	0.32(5)	115	0.38(6)	–	–	147
$B_g^{(5)}$	Nonlinear	127.5	Nonlinear	Nonlinear	140	Nonlinear	−0.6	140	176
$B_g^{(4)}$	2.45	158.8	2.33	1.95(7)	178	1.50(6)	3.4*	178*	200
$E_g^{(4)}$	2.10	184.1	1.72	2.29(7)	189	1.66(6)	2.1	190	188
$A_g^{(3)}$	0.89	229.3	0.59	0.86(5)	236	0.50(3)	1.0	236	244
$E_g^{(3)}$	2.12	297.1	1.08	2.36(8)	309	1.05 (4)	2.8	307	321
$A_g^{(2)}$	2.18	319.5	1.03	2.88(7)	348	1.13(3)	2.3	350	350
$B_g^{(3)}$	2.66	343.4	1.17	1.90(11)	374	0.70(4)	1.0	370	368
$B_g^{(2)}$	2.75	383.8	1.08	3.19(8)	401	1.09(3)	2.6	407	417
$E_g^{(2)}$	2.86	402.5	1.07	3.10(9)	428	0.99(3)	1.7	432	435
$E_g^{(1)}$	3.04	742.8	0.62	3.99 (9)	744	0.73(2)	2.8	745	748
$B_g^{(1)}$	2.50	791.5	0.48	2.97(14)	808	0.50(2)	1.6	804	809
$A_g^{(1)}$	3.47	810.9	0.65	3.33(8)	833	0.55(2)	3.2	833	831

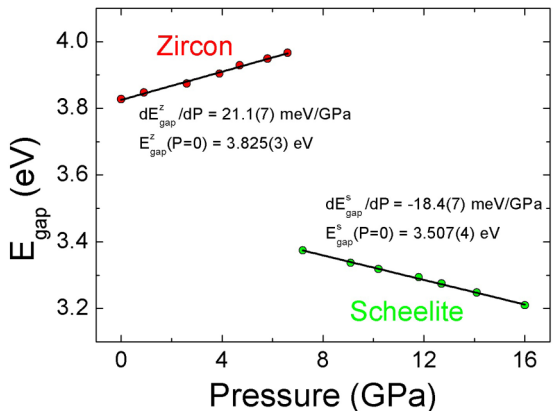

FIG. 8. Band-gap energy vs pressure. Red and green circles stand for the experimental data obtained for the zircon and scheelite phases, respectively. Solid lines represent the linear fit to both sets of data. The parameters obtained are indicated in the figure as well.

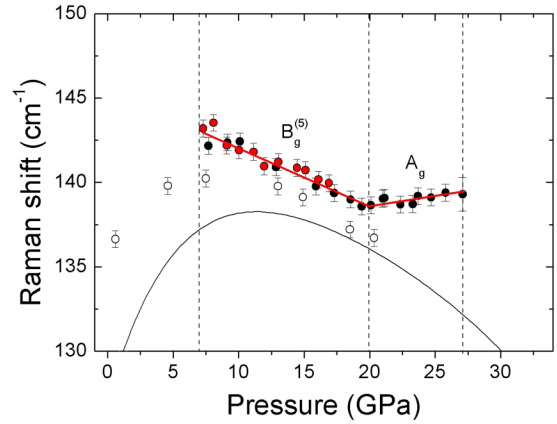

FIG. 9. Pressure dependence of the scheelite soft mode $B_{1g}^{(5)}$ and its transformation into one A_g fergusonite mode near 20 GPa. The meaning of the symbols is the same as that used in Fig. 6. The black solid curve represents the theoretical dependence on pressure of the scheelite phase $B_{1g}^{(5)}$ mode. Red solid straight lines on experimental data symbols are a guide to the eye.

by some partial decomposition. In our case, we do not observe any peaks that could be associated with V_2O_5, which suggests that nonoptimal hydrostaticity can trigger some partial decomposition of RVO_4 compounds under high pressure.

During these experiments, we observed a subtle change in the color of the sample before and after the zircon-scheelite phase transition. Thus, we additionally performed optical-absorption measurements on single-crystal zircon-type $GdVO_4$ up to 16 GPa. The evolution of the absorption spectra under pressure is shown in Fig. S1. From these experimental data we deducted the pressure dependence of the band-gap energy E_{gap} of the zircon and scheelite phases, which is shown in Fig. 8. It can be observed that at the transition point a band-gap collapse of ~ 0.6 eV takes place. This constitutes a reasonable explanation for the color change of the sample. Also, as it can be seen in Fig. 8, when pressure is applied, the forbidden band widens in the zircon phase whereas it narrows in the scheelite phase. The pressure coefficients are indicated within Fig. 8. Similar behavior has been reported for other zircon-type RVO_4 compounds [76,77]. A deeper discussion of these data can be seen in the Supplemental Material [78] (see also references [79–82] therein).

Figure 9 shows how the Raman peak associated with the $B_g^{(5)}$ mode of the scheelite phase shifts towards low frequencies when the sample is compressed. Beyond 20 GPa, the behavior of this peak is the opposite. Previous studies on scheelite structured oxides have reported that the $B_g^{(5)}$ mode shows no discontinuity in frequency with a fergusonite A_g mode, and whereas the former softens with pressure, the latter hardens just after the transition point. This mechanism is considered characteristic of a second-order scheelite-to-fergusonite phase transition [83]. These results and those obtained in the XRD experiments constitute evidence of a phase transition near 20 GPa from scheelite- to fergusonite-type $GdVO_4$. In Fig. 6(b) the spectrum obtained in the experiment at 22.4 GPa is compared with the calculated position of the fergusonite peaks at the same pressure, showing a reasonably good agreement between both. These calculations were made assuming the same unit cell as the one obtained in the XRD data analysis at 22.4 GPa ($a = 4.8933$ Å, $b = 10.9367$ Å, $c = 4.8160$ Å, $\beta = 91.06°$). According to our calculations, this transition would be characterized by a small splitting of the scheelite $E_g^{(1-5)}$ mode peaks due to the lower symmetry of the postscheelite phase. However, the effect of the distortion is small, and the associated splitting cannot be directly inferred from our measured Raman spectra. Besides this, the progressive broadening of the Raman peaks caused by the deterioration of the hydrostatic conditions could contribute to make these effects even more imperceptible. In order to not misinterpret the experiments, we decided to analyze the evolution of those peaks as if they were single. More accurately, in Fig. 6(b) we are not explicitly representing the pressure evolution of the fergusonite phase phonons but the evolution of the Raman spectra peaks observed above 20 GPa.

Under further compression, at 29.3 GPa additional changes in the Raman spectrum are observed. Beyond 32.6 GPa, the fergusonite Raman peaks vanish and only some broad bands can be seen in the spectra. We suggest that this could be a fourth high-pressure phase of $GdVO_4$. Other studies on rare-earth orthovandates, such as $TbVO_4$ [53], suggested the existence of a higher symmetry phase, an orthorhombic structure with *Cmca* symmetry. Considering this scenario, the transition would involve a coordination increase of both V and Gd atoms at the transition point and a huge volume collapse of 11.8%. The increase in V coordination from 4 to 6 would imply a larger polyhedral unit and consequently, a weaker V-O bonding, which would be induced in a smaller frequency of the dominating stretching mode. In fact, the most intense band of the fourth HP phase appears just at the low-wave-number side of the fergusonite most intense peak, which is the one associated to the A_g stretching mode. This seems to be a coherent scenario, albeit it is only a conjecture and further experiments are needed to confirm this hypothesis. However, in this study we will assume hereon that the fourth phase is the previously reported orthorhombic structure. The existence of a high number of Raman-active modes (36 at the Γ point) and the presence of deviatoric stresses caused by a progressive loss

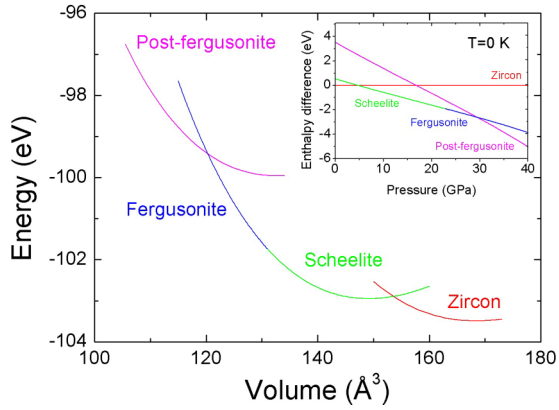

FIG. 10. Calculated energy-volume curves for different structures of $GdVO_4$. The inset shows the difference in enthalpy respect to the zircon phase. Calculations were carried out neglecting temperature effects ($T = 0$ K).

of hydrostaticity may be the main causes of the appearance of broad bands. Consequently, the pressure evolution of these modes cannot be extracted from the experiments. It is worth stressing that, at the moment we reached the third phase transition, we realized that the laser beam used for exciting the ruby was absorbed by the sample. In particular, the sample becomes opaque, having a bright gray color. This implies that the band gap has moved from the visible to the near infrared as happens in $SrCrO_4$ [84]. However, the fact that the reflectivity of the samples is not enhanced indicates that the band-gap decrease does not involve a pressure-driven metallization, contradicting previous predictions [81].

In Fig. 6(c) Raman spectra obtained under pressure release are shown. Upon decompression, subtle peaks seem to arise at 22.6 GPa and become more evident at 20.3 GPa. As the sample is decompressed, the orthorhombic postfergusonite structure bands start to decrease in intensity, and the typical Raman peak distribution of the scheelite phase reappears. Hence, we can state that there is a phase transition near 22.6 GPa. This pressure is very close to the scheelite-to-fergusonite phase transition upon compression, and therefore, it is reasonable to claim that the obtained phase is scheelite- and not fergusonite-type $GdVO_4$. At 0.6 GPa, the scheelite phase is recovered, showing the irreversible character of the zircon-to-scheelite transition. In addition to this, two postfergusonite $GdVO_4$ bands remain (asterisks); i.e., the recovered sample contains scheelite-type as well as orthorhombic $GdVO_4$, both in a metastable state.

C. *Ab initio* calculations

Figure 10 shows the calculated energy-volume curves for the zircon-, scheelite-, fergusonite-, and post-fergusonite-type $GdVO_4$. The inset of this figure shows the enthalpy difference vs pressure for these phases, taking the zircon phase as a reference. In addition, in Table IV theoretical structural parameters of the four polymorphs are shown. According to Fig. 10, a phase transition from zircon to scheelite is predicted to occur at 4.8 GPa. This is a first-order reconstructive transition which particularly involves a large volume collapse of 10.9%, according to the energy-volume calculations. Nyman *et al.* [85] and Flórez *et al.* [86] have described the structural relation between these two structures. Since this is a first-order reconstructive transition, it has been suggested that the zircon-to-scheelite transition has a large kinetic barrier, and thus, these theoretical calculations tend to underestimate the experimental transition pressure.

TABLE IV. Theoretical structural parameters of $GdVO_4$ phases. Since the fergusonite structure reduces to scheelite in our calculations, the cell parameters were fixed to those obtained at 22.4 GPa in the XRD experiments.

Atom	Site	x	y	z
Zircon at 0 GPa; $a = b = 7.22610$ Å, $c = 6.35814$ Å				
O	16h	0	−0.06618	0.79907
V	4b	0	0.25	0.375
Gd	4a	0	0.75	0.125
Scheelite at 14.181 GPa; $a = b = 4.96269$ Å, $c = 10.96299$ Å				
O	16f	0.65091	0.50346	0.29159
V	4a	0	0.25	0.125
Gd	4b	0	0.25	0.625
Fergusonite at 22.4 GPa; $a = 4.89330$ Å, $b = 10.93670$ Å, $c = 4.81600$ Å, $\beta = 91.06°$				
O_1	8f	0.00104	0.21022	0.15253
O_2	8f	0.90564	0.45963	0.24678
V	4e	0.25	0.87632	0
Gd	4e	0.25	0.37511	0
Postfergusonite at 31.8 GPa; $a = 7.37379$ Å, $b = 12.23432$ Å, $c = 4.92167$ Å				
O_1	8f	0	0.08762	0.07106
O_2	8d	0.65227	0	0
O_3	8f	0	0.20808	0.50645
O_4	8e	0.25	0.34707	0.25
V	8f	0	0.41012	0.21704
Gd	8e	0.25	0.15843	0.25

TABLE V. Stiffness matrix elements of different zircon-type RVO_4 compounds at zero pressure.

Elastic constant	$SmVO_4$ [60]	$GdVO_4$ (this work)	$TbVO_4$ [90]	$DyVO_4$ [90,91]	$HoVO_4$ [92]	$ErVO_4$ [93]
	Theoretical		Experimental			
C_{11}	212	227.2	240(2)	242(2)	246.4 (230 K)	256.6(5.1)
C_{12}	37	45.6	55(3)	50(4)	–	53(3)
C_{13}	76	83.9	–	–	–	79(6)
C_{33}	286.6	297.8	–	–	310.5 (190 K)	313(6)
C_{44}	40.8	43.5	–	–	48.5 (250 K)	50.1(1.0)
C_{66}	13.6	16.5	13.1(2.0)	15.0(0.5)	16.07 (250 K)	17.7(0.9)

In order to analyze the evolution of the zircon phase modes as well as the possible existence of any dynamical instability, we performed lattice-dynamics calculations. Besides the Raman-active modes (Fig. 7), we also calculated the infrared active and silent modes, which are shown in Figs. S2 and S3, respectively, for both (a) zircon and (b) scheelite phases (see Supplemental Material [78]). All the IR modes of the zircon phase harden with pressure except an E_u mode near $\sim 300\,\mathrm{cm}^{-1}$ which remains approximately constant (less than 1% of variation). In the scheelite phase, only two modes soften with pressure. These have E_u ($\sim$150 cm^{-1} at 0 GPa) and A_u ($\sim$250 cm^{-1} at 0 GPa) symmetries. As a consequence of this, the second one shows a mode crossover with an E_u mode ($\sim$200 cm^{-1} at 0 GPa) at 21 GPa. Regarding the zircon phase silent modes, two modes harden, one remains constant, and two of them soften with pressure. In particular, Fig. S3(a) shows that one silent mode B_{1u} has a strong nonlinear dependence with pressure. This mode corresponds to rotations of the VO_4 mode, and its frequency decreases with pressure and reaches the value of zero at $\sim$8.2 GPa. Other vanadates [53] and isomorphic compounds such as zircon-type $TmPO_4$ [87] also show this mode softening. The vibration pattern of this mode is shown in Fig S4 [78].

In addition, we calculated the elastic properties of both zircon- and scheelite-type $GdVO_4$. The elastic constants of the $GdVO_4$ zircon and scheelite phases, in the Voigt notation [88,89], are summarized in Tables V and VI, together with other empirical and theoretical values reported in literature for different zircon and scheelite-type RVO_4 compounds, respectively [16,60,90–93]. Regarding the zircon phase (Table V), our calculated elastic constants are in a reasonably good agreement with the general trend, although they seem to be slightly underestimated. In Table VI we compare present and previous results [60] obtained for $SmVO_4$ and $GdVO_4$ using the GGA + U and LSDA + U [16] approximations. These calculations were performed with the VASP and CASTEP software packages, respectively. The elastic constants of $SmVO_4$ and $GdVO_4$ are more similar in our calculations than those reported in Ref. [16]. Also, Table V shows that some of the values reported in Ref. [16] are quite large for both compounds.

TABLE VI. Stiffness matrix elements of different scheelite-type RVO_4 compounds at zero pressure.

Elastic constant	$SmVO_4$ [60]	$SmVO_4$ [16]	$GdVO_4$ (this work)	$GdVO_4$ [16]
C_{11}	218	192	229.5	279
C_{12}	114.4	77	115.5	146
C_{13}	99.5	92	97.9	129
C_{33}	196.3	187	200.5	251
C_{44}	53.4	57	54.9	79
C_{66}	68.1	96	69.8	85
C_{16}	−21.8	−56	−22.5	−22

When a nonzero stress is applied to the structure, the stiffness coefficients B_{ijkl} should be used:

$$B_{ijkl} = C_{ijkl} + 1/2[\delta_{ik}\sigma_{jl} + \delta_{jk}\sigma_{il} + \delta_{il}\sigma_{jk} + \delta_{jl}\sigma_{ik} - 2\delta_{kl}\sigma_{ij}], \quad (1)$$

where C_{ijkl} represent the elastic constants evaluated at the present stressed state, σ_{ij} stand for the external stresses, and δ_{ij} is the Kronecker delta [90]. Our calculations are performed simulating hydrostatic conditions ($\sigma_{11} = \sigma_{22} = \sigma_{33} = -P$). The evolution of these parameters with pressure is displayed in Fig. 11 for both phases. As we can see in the inset of Fig. 11(a), the zircon phase shows a mechanical instability at 9.6 GPa, since at this pressure one of the stiffness matrix eigenvalues becomes zero. Furthermore, above this pressure $B_{66} < 0$, which violates one of the Born stability criteria [88,94–97] for a tetragonal I structure (point groups $4mm$, 422, $-42m$, and $4/mmm$). Calculations have shown that beyond 22.8 GPa the stiffness matrix of the scheelite structure

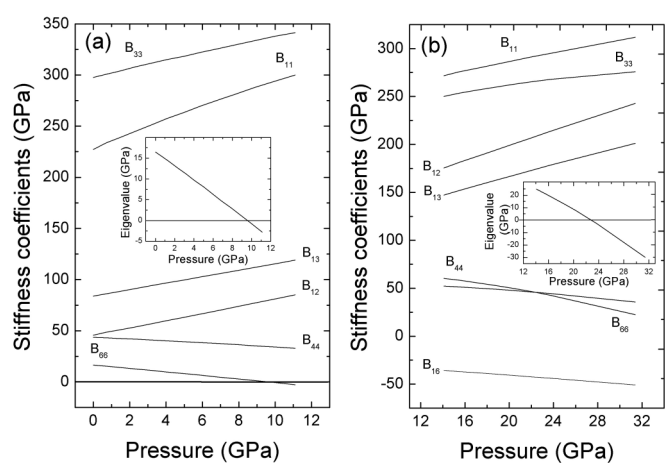

FIG. 11. Evolution of the stiffness matrix coefficients of the (a) zircon and (b) scheelite phases with pressure. Insets: Pressure dependence eigenvalue that becomes negative, for each phase, which indicates the presence of a mechanical instability. This situation occurs at 9.6 and 22.8 GPa for the zircon and scheelite phases, respectively.

TABLE VII. Calculated elastic moduli K, E, and G (GPa), K/G ratio, and Poisson's ratio (ν) in the Voigt, Reuss, and Hill approximations for the zircon and scheelite phases of $GdVO_4$. The values shown were calculated at zero pressure. The experimental and theoretical values reported by Huang *et al.* [16] for scheelite-type $GdVO_4$ are also included.

Phase	Approximation	K	E	G	ν	K/G
Zircon	Voigt	131.0	148.5	56.6	0.311	2.31
	Reuss	126.1	105.3	38.7	0.361	3.26
	Hill	128.5	127.2	47.6	0.335	2.70
Scheelite	Voigt	142.5	155.8	59.1	0.318	2.41
	Reuss	141.1	147.3	55.5	0.326	2.54
	Hill	141.8	151.6	57.3	0.322	2.47
	Hill [16]	179	198	75	0.320	2.40
	Experimental [16]	140	175	68	0.290	2.10

is not positive-definite and thus the crystal is mechanically unstable. In particular, one of the eigenvalues becomes zero at 22.8 GPa, as displayed in the inset of Fig. 11(b). This is equivalent to saying that one of the generalized Born criterion for a tetragonal II (point groups 4, -4, and $4/m$) structure, in particular, $2B_{16}^2 < B_{66}(B_{11} - B_{12})$ [88,94–97], is violated at this pressure. It should be noted that even if the scheelite phase has a tetragonal point symmetry as does the zircon phase, it does not share the Born stability criteria with the zircon phase. The tetragonal I class has six independent elastic constants, while the tetragonal II class has an extra elastic constant, C_{16}, and must fulfill an extra stability criteria $2B_{16} < B_{66}(B_{11} - B_{12})$ [88,97] related with this elastic constant. The mechanical instability found in Ref. [98] for the scheelite phase is stated in terms of B_{66}, whereas $2B_{16}^2 < B_{66}(B_{11} - B_{12})$ is not analyzed.

We can deduce which is the direction of the deformation by calculating the eigenvector associated with the eigenvalue that becomes negative over 22.8 GPa. In fact, the calculated eigenvector is (−0.4195, 0.4195, 0, 0, 0.8050) at 23.7 GPa, which corresponds to a deformation within the *ab* plane of the structure. As a consequence of this distortion, the γ angle decreases, the a parameter contracts, and the b parameter expands. These changes are compatible with a monoclinic distortion of the scheelite structure. Such conclusions strongly reinforce the idea of a phase transition from scheelite- to fergusonite-type $GdVO_4$.

The bulk (K), shear (G), and Young (E) moduli as well as the Poisson's ratio (ν) in the Voigt [99], Reuss [100], and Hill [101] approximations can be expressed as combinations of the stiffness coefficients. All these parameters are summarized in Table VII for both zircon- and scheelite-type $GdVO_4$ at zero-pressure conditions. In the same table we included the theoretical and experimental values of K, G, E, and ν obtained by Huang *et al.* [16] for the sake of comparison. The values of the bulk moduli of the zircon and scheelite phases calculated at 0 GPa are in good agreement with the experimental values shown in Table I and reported by Huang *et al.* [16]. Pugh [102] proposed an empirical relationship between and plastic deformation properties of materials which can be expressed as the K/G ratio (also shown in Table VII). According to that study, a material is considered ductile when $K/G > 1.75$ and brittle otherwise. We found that both zircon- and scheelite-type $GdVO_4$ are ductile at zero pressure, having similar K/G values.

Finally, we also report the calculated BM EOS parameters of the postfergusonite phase, which are shown in Table I. Apparently, this structure is more compressible than the scheelite phase (see Table I), which is in apparent contradiction with its higher density. This phenomenon has been studied in literature and two possible hypotheses have been suggested. The first one claims that, according to Hofmeister [103], the decrease observed in the bulk modulus is directly related to the weakening of the interatomic bonds, caused by the increment of the average interatomic distances after the transition. The second one claims that the smaller bulk modulus can be explained as a consequence of a localized-to-delocalized electronic transition. Studies on lanthanides [104] have shown that pressure induces an f-electron delocalization. This would produce a weaker Gd-O bond, and so the postfergusonite phase would be slightly more compressible. However, these hypotheses need to be tested by future studies.

IV. CONCLUSIONS

We report an experimental and theoretical study on the behavior of $GdVO_4$ under high pressure. We studied the different polymorphs and their stability from a mechanical and dynamical perspective. The Raman-active modes of the different polymorphs have been accurately characterized. Our study clearly confirms that there is a first zircon-to-scheelite phase transition between 6.6 and 7.3 GPa. After this transition, the scheelite phase remains stable up to 20 GPa. Above this pressure, recognizable changes in the crystal structure take place. According to our calculations, this is compatible with a mechanical instability that leads to a monoclinic structural distortion. Our experiments confirm this, suggesting the fergusonite structure as the third polymorph. Upon further compression, substantial changes occur above 29 GPa. As our *ab initio* calculations indicate, these changes are compatible with a third phase transition from the fergusonite structure to an orthorhombic postfergusonite structure. This phase is found to have a small band gap in the IR region and its compressibility is predicted to be higher than that of the previous phase. When pressure is released, this structure shows a 6-GPa hysteresis, transforming back directly to the scheelite structure, which arises at approximately 22.9 GPa. After complete decompression, the recovered sample is composed by scheelite-type $GdVO_4$ and a small fraction of the postfergusonite structure, both in a metastable state.

ACKNOWLEDGMENTS

This work was supported by the Spanish Ministry of Science, Innovation and Universities under Grant No. MAT2016-75586-C4-1/3-P and by the Generalitat Valenciana under Grant Prometeo/2018/123 (EFIMAT). T.M. and D.S. acknowledge the Spanish Ministry of Science, Innovation and Universities for the BES-2017-079651 predoctoral fellowship and the RyC-2014-15643 Ramon y Cajal Senior grant, respectively. The authors thank the ALBA-CELLS synchrotron for providing beam time for the XRD experiments (Project No. 2016081779).

[1] J. Liu, H. Zhang, Z. Wang, J. Wang, Z. Shao, M. Jiang, and H. Weber, Continuous-wave and pulsed laser performance of Nd:$LuVO_4$ crystal, Opt. Lett. **29**, 168 (2004).

[2] A. K. Levine and F. C. Palilla, A new, highly efficient red-emitting cathodoluminescent phosphor (YVO_4:Eu) for color television, Appl. Phys. Lett. **5**, 118 (1964).

[3] Y. Fujimoto, T. Yanagida, Y. Yokota, V. Chani, V. V. Kochurikhin, and A. Yoshikawa, Comparative study of optical and scintillation properties of YVO_4, $Lu_{0.5}Y_{0.5}VO_4$, and $LuVO_4$ single crystals, Nucl. Instrum. Methods Phys. Res., Sect. A **635**, 53 (2011).

[4] M. Oshikiri, J. Ye, and M. Boero, Inhomogeneous RVO photocatalyst systems (R = Y, Ce, Pr, Nd, Sm, Eu, Gd, Tb, Dy, Ho, Er, Tm, Yb, Lu), J. Phys. Chem. C **118**, 8331 (2014).

[5] D. Errandonea and F. J. Manjon, Pressure effects on the structural and electronic properties of ABX_4 scintillating crystals, Prog. Mater. Sci. **53**, 711 (2008).

[6] H. D. Jiang, H. J. Zhang, J. Y. Wang, H. R. Xia, X. B. Hu, B. Teng, and C. Q. Zhang, Optical and laser properties of Nd:$GdVO_4$ crystal, Opt. Commun. **198**, 447 (2001).

[7] T. T. Basiev, S. V. Vassiliev, V. A. Konjushkin, V. V. Osiko, A. I. Zagumennyĭ, Y. D. Zavartsev, I. A. Kutovoi, and I. A. Shcherbakov, Diode pumped 500-picosecond Nd:$GdVO_4$ Raman laser, Laser Phys. Lett. **1**, 237 (2004).

[8] Y. F. Chen, Efficient 1521-nm Nd:$GdVO_4$ Raman laser, Opt. Lett. **29**, 2632 (2004).

[9] H. Zhang, X. Meng, J. Liu, L. Zhu, C. Wang, Z. Shao, J. Wang, and Y. Liu, Growth of lowly Nd doped $GdVO_4$ single crystal and its laser properties, J. Cryst. Growth **216**, 367 (2000).

[10] A. I. Zagumennyĭ, V. G. Ostroumov, I. A. Shcherbakov, T. Jensen, J. P. Meyen, and G. Huber, The Nd:$GdVO_4$ crystal: A new material for diode-pumped lasers, Sov. J. Quantum Electron. **22**, 1071 (1992).

[11] B. N. Mahalley, S. J. Dhoble, R. B. Pode, and G. Alexander, Photoluminescence in $GdVO_4$: Bi^{3+}, Eu^{3+} red phosphor, Appl. Phys. A **70**, 39 (2000).

[12] O. V. Voloshina, V. N. Baumer, V. G. Bondar, D. A. Kurtsev, T. E. Gorbacheva, I. M. Zenya, A. V. Zhulov, and O. T. Sidletskiy, Growth and scintillation properties of gadolinium and yttrium orthovanadate crystals, Nucl. Instrum. Methods Phys. Res., Sect. A **664**, 299 (2012).

[13] T. Marqueño, V. Monteseguro, F. Cova, D. Errandonea, D. Santamaria-Perez, E. Bandiello, and M. Bettinelli, High-pressure phase transformations in $NdVO_4$ under hydrostatic conditions: A structural powder X-ray diffraction study, J. Phys.: Condens. Matter **31**, 235401 (2019).

[14] V. Panchal, S. López-Moreno, D. Santamaría-Pérez, D. Errandonea, F. J. Manjón, P. Rodríguez-Hernandez, A. Muñoz, S. N. Achary, and A. K. Tyagi, Zircon to monazite phase transition in $CeVO_4$: X-ray diffraction and Raman-scattering measurements, Phys. Rev. B **84**, 024111 (2011).

[15] C. C. Zhang, Z. M. Zhang, R. C. Dai, Z. P. Wang, J. W. Zhang, and Z. J. Ding, High-pressure Raman and luminescence study on the phase transition of $GdVO_4$:Eu^{3+} microcrystals, J. Phys. Chem. C **114**, 18279 (2010).

[16] Z. Huang, L. Zhang, and W. Pan, Synthesis, lattice dynamics, and mechanical properties of a high-pressure scheelite phase of RVO_4, Inorg. Chem. **51**, 11235 (2012).

[17] F. Hong, B. Yue, Z. Cheng, H. Shen, K. Yang, X. Hong, B. Chen, and H. K. Mao, Pressure-enhanced light emission and its structural origin in Er:$GdVO_4$, Appl. Phys. Lett. **110**, 021903 (2017).

[18] B. Yue, F. Hong, S. Merkel, D. Tan, J. Yan, B. Chen, and H. K. Mao, Deformation Behavior Across the Zircon-Scheelite Phase Transition, Phys. Rev. Lett. **117**, 135701 (2016).

[19] D. Santamaria-Perez, L. Gracia, G. Garbarino, A. Beltran, R. Chulia-Jordan, O. Gomis, D. Errandonea, C. Ferrer-Roca, D. Martinez-Garcia, and A. Segura, High-pressure study of the behavior of mineral barite by x-ray diffraction, Phys. Rev. B **84**, 054102 (2011).

[20] A. B. Garg, D. Errandonea, P. Rodríguez-Hernández, S. López-Moreno, A. Muñoz, and C. Popescu, High-pressure structural behavior of $HoVO_4$: Combined XRD experiments and ab initio calculations, J. Phys.: Condens. Matter **26**, 265402 (2014).

[21] A. B. Garg, D. Errandonea, P. Rodríguez-Hernández, and A. Muñoz, ScVO under non-hydrostatic compression: A new metastable polymorph. J. Phys.: Condens. Matter **29**, 055401 (2016).

[22] V. Panchal, F. J. Manjón, D. Errandonea, P. Rodriguez-Hernandez, J. López-Solano, A. Muñoz, and A. K. Tyagi, High-pressure study of $ScVO_4$ by Raman scattering and *ab initio* calculations, Phys. Rev. B **83**, 064111 (2011).

[23] D. Errandonea, C. Popescu, S. N. Achary, A. K. Tyagi, and M. Bettinelli, In situ high-pressure synchrotron X-ray diffraction study of the structural stability in $NdVO_4$ and $LaVO_4$, Mat. Res. Bull. **50**, 279 (2014).

[24] C. Goutaudier, F. S. Ermeneux, M. T. Cohen-Adad, R. Moncorgé, M. Bettinelli, and E. Cavalli, LHPG and flux growth of various Nd:YVO_4 single crystals: a comparative characterization. Mater. Res. Bull. **33**, 1457 (1998).

[25] D. Errandonea and A. B. Garg, Recent progress on the characterization of the high-pressure behavior of AVO_4 orthovanadates, Prog. Mater. Sci. **97**, 123 (2018).

[26] A. Dewaele, P. Loubeyre, and M. Mezouar, Equations of state of six metals above 94 GPa, Phys. Rev. B **70**, 094112 (2004).

[27] S. Klotz, J. C. Chervin, P. Munsch, and G. Le Marchand, Hydrostatic limits of 11 pressure transmitting media, J. Phys. D: Appl. Phys. **42**, 075413 (2009).

[28] D. Errandonea, R. Boehler, S. Japel, M. Mezouar, and L. R. Benedetti, Structural transformation of compressed solid Ar: An x-ray diffraction study to 114 GPa, Phys. Rev. B **73**, 092106 (2006).

[29] D. Errandonea, A. Muñoz, and J. Gonzalez-Platas, Comment on "High-pressure x-ray diffraction study of YBO_3/Eu^{3+}, $GdBO_3$, and $EuBO_3$: Pressure-induced amorphization in $GdBO_3$" J. Appl. Phys. **115**, 216101 (2014).

[30] D. Errandonea, Exploring the properties of MTO_4 compounds using high-pressure powder x-ray diffraction, Cryst. Res. Technol. **50**, 729 (2015).

[31] F. Fauth, I. Peral, C. Popescu, and M. Knapp, The new material science powder diffraction beamline at ALBA synchrotron, Powder Diffr. **28**, S360 (2013).

[32] C. Prescher and V. B. Prakapenka, DIOPTAS: A program for reduction of two-dimensional X-ray diffraction data and data exploration, High Pressure Res. **35**, 223 (2015).

[33] W. Kraus and G. Nolze, POWDER CELL—A program for the representation and manipulation of crystal structures and calculation of the resulting X-ray powder patterns, J. Appl. Crystallogr. **29**, 301 (1996).

[34] J. Rodriguez-Carvajal, Recent advances in magnetic structure determination by neutron powder diffraction, Physica B **192**, 55 (1993).

[35] D. Errandonea, D. Santamaria-Perez, V. Grover, S. N. Achary, and A. K. Tyagi, High-pressure x-ray diffraction study of bulk and nanocrystalline $PbMoO_4$, J. Appl. Phys. **108**, 073518 (2010).

[36] A. LeBail, H. Duroy, and J. L. Fourquet, *Ab-initio* structure determination of $LiSbWO_6$ by X-ray powder diffraction, Mater. Res. Bull. **23**, 447 (1988).

[37] H. K. Mao, J. Xu, and P. M. Bell, Calibration of the ruby pressure gauge to 800 kbar under quasi-hydrostatic conditions, J. Geophys. Res. **91**, 4673 (1986).

[38] G. Kresse and J. Furthmuller, Efficient iterative schemes for ab initio total-energy calculations using a plane-wave basis set, Phys. Rev. B **54**, 11169 (1996).

[39] G. Kresse and D. Joubert, From ultrasoft pseudopotentials to the projector augmented-wave method, Phys. Rev. B **59**, 1758 (1999).

[40] P. Hohenberg and W. Kohn, Density functional theory (DFT), Phys. Rev. **136**, B864 (1964).

[41] P. E. Blöchl, Projector augmented-wave method, Phys. Rev. B **50**, 17953 (1994).

[42] J. P. Perdew, K. Burke, and M. Ernzerhof, Generalized Gradient Approximation Made Simple, Phys. Rev. Lett. **77**, 3865 (1996).

[43] S. L. Dudarev, G. A. Botton, S. Y. Savrasov, C. J. Humphreys, and A. P. Sutton, Electron-energy-loss spectra and the structural stability of nickel oxide: An LSDA+ U study, Phys. Rev. B **57**, 1505 (1998).

[44] M. Topsakal, C. Leighton, and R. Wentzkovitch, First-principles study of crystal and electronic structure of rare-earth cobaltites, J. Appl. Phys. **119**, 244310 (2016).

[45] K. Parlinski, Computer code PHONON, ⟨http://wolf.ifj.edu.pl/phonon/⟩.

[46] H. Saqib, S. Rahman, D. Errandonea, R. A. Susilo, A. Jorge-Montero, P. Rodríguez-Hernández, A. Muñoz, Yan Sun, Zhiqiang Chen, Ning Dai, and Bin Chen, Giant conductivity enhancement: Pressure-induced semiconductor-metal phase transition in $Cd_{0.90}Zn_{0.10}Te$, Phys. Rev. B **99**, 094109 (2019).

[47] W. O. Milligan and L. W. Vernon, Crystal structure of heavy metal orthovanadates, J. Phys. Chem. **56**, 145 (1952).

[48] A. Szczeszak, T. Grzyb, Z. Śniadecki, N. Andrzejewska, S. Lis, M. Matczak, G. Nowaczyk, S. Jurga, and B. Idzikowski, Structural, spectroscopic, and magnetic properties of Eu^{3+}-doped $GdVO_4$ nanocrystals synthesized by a hydrothermal method, Inorg. Chem. **53**, 12243 (2014).

[49] Z. Huang, L. Zhang, J. Feng, X. Cui, and W. Pan, Electronic, elastic and optical properties of zircon $GdVO_4$ investigated from experiments and LSDA + U, J. Alloys Compd. **538**, 56 (2012).

[50] G. K. Williamson and W. H. Hall, X-ray line broadening from filed aluminium and Wolfram, Acta Metall. **1**, 22 (1953).

[51] J. Ruiz-Fuertes, D. Martínez-García, T. Marqueño, D. Errandonea, S. G. MacLeod, T. Bernert, E. Haussühl, D. Santamaria-Perez, J. Ibáñez, A. Mallavarapu, S. N. Achary, C. Popescu, and M. Bettinelli. High-pressure high-temperature stability and thermal equation of state of zircon-type erbium vanadate, Inorg. Chem. **57**, 14005 (2018).

[52] A. B. Garg and D. Errandonea, High-pressure powder x-ray diffraction study of $EuVO_4$, J. Solid State Chem. **226**, 147 (2015).

[53] D. Errandonea, F. J. Manjón, A. Muñoz, P. Rodríguez-Hernández, V. Panchal, S. N. Achary, and A. K. Tyagi, High-pressure polymorphs of $TbVO_4$: A Raman and *ab initio* study, J. Alloys Compd. **577**, 327 (2013).

[54] R. Mittal, A. B. Garg, V. Vijayakumar, S. N. Achary, A. K. Tyagi, B. K. Godwal, E. Busetto, A. Lausi, and S. L. Chaplot, Investigation of the phase stability of $LuVO_4$ at high pressure using powder x-ray diffraction measurements and lattice dynamical calculations, J. Phys.: Condens. Matter **20**, 075223 (2008).

[55] A. K. Arora, Tomoko Sato, Taku Okada, and Takehiko Yagi, High-pressure amorphous phase of vanadium pentaoxide, Phys. Rev. B **85**, 094113 (2012).

[56] M. Pravica, L. Bai, D. Sneed, and C. Park, Measurement of the energy dependence of X-ray-induced decomposition of potassium chlorate, J. Phys. Chem. A **117**, 2302 (2013).

[57] D. Errandonea, S. N. Achary, J. Pellicer-Porres, and A. K. Tyagi, Pressure-induced transformations in $PrVO_4$ and $SmVO_4$ and isolation of high-pressure metastable phases, Inorg. Chem. **52**, 5464 (2013).

[58] A. B. Garg, R. Rao, T. Sakuntala, B. N. Wani, and V. Vijayakumar, Phase stability of $YbVO_4$ under pressure: In situ x-ray and Raman spectroscopic investigations, J. Appl. Phys. **106**, 063513 (2009).

[59] F. Birch, Elasticity and constitution of the Earth's interior, J. Geophys. Res. **57**, 227 (1952).

[60] C. Popescu, A. B. Garg, D. Errandonea, J. A. Sans, P. Rodriguez-Hernández, S. Radescu, A. Muñoz, S. N. Achary, and A. K. Tyagi, Pressure-induced phase transformation in zircon-type orthovanadate $SmVO_4$ from experiment and theory, J. Phys.: Condens. Matter **28**, 035402 (2016).

[61] W. Paszkowicz, J. López-Solano, P. Piszora, B. Bojanowski, A. Mujica, A. Muñoz, Y. Cerenius, S. Carlson, and H. Dąbkowska, Equation of state and electronic properties of $EuVO_4$: A high-pressure experimental and computational study, J. Alloys Compd. **648**, 1005 (2015).

[62] W. Paszkowicz, O. Ermakova, J. Lopez-Solano, A. Mujica, A. Munoz, R. Minikayev, C. Lathe, S. Gierlotka, I. Nikolaenko, and H. Dabkowska, Equation of state of zircon-and scheelite-type dysprosium orthovanadates: A combined experimental and theoretical study, J. Phys.: Condens. Matter **26**, 025401 (2013).

[63] D. Errandonea, R. S. Kumar, X. Ma, and C. Tu, High-pressure X-ray diffraction study of $SrMoO_4$ and pressure-induced structural changes, J. Solid State Chem. **181**, 355 (2008).

[64] R. Lacomba-Perales, D. Errandonea, Y. Meng, and M. Bettinelli, High-pressure stability and compressibility of APO_4 (A= La, Nd, Eu, Gd, Er, and Y) orthophosphates: An x-ray diffraction study using synchrotron radiation, Phys. Rev. B **81**, 064113 (2010).

[65] I. Guedes, Y. Hirano, M. Grimsditch, N. Wakabayashi, C. K. Loong, and L. A. Boatner, Raman study of phonon modes in $ErVO_4$ single crystals, J. Appl. Phys. **90**, 1843 (2001).

[66] Y. K. Voron'ko, V. E. Shukshin, A. I. Zagumennyĭ, Y. D. Zavartsev, and S. A. Kutovoĭ, Raman spectroscopic study of structural disordering in YVO_4, $GdVO_4$, and $CaWO_4$ crystals, Phys. Solid State **51**, 1886 (2009).

[67] J. Pellicer-Porres, D. Vázquez-Socorro, S. López-Moreno, A. Muñoz, P. Rodríguez-Hernández, D. Martínez-García, S. N. Achary, A. J. E. Rettie, and C. B. Mullins, Phase transition systematics in $BiVO_4$ by means of high-pressure–high-temperature Raman experiments, Phys. Rev. B **98**, 214109 (2018).

[68] A. Sanson, M. Giarola, B. Rossi, G. Mariotto, E. Cazzanelli, and A. Speghini, Vibrational dynamics of single-crystal YVO_4 studied by polarized micro-Raman spectroscopy and ab initio calculations, Phys. Rev. B **86**, 214305 (2012).

[69] F. J. Manjón, P. Rodríguez-Hernández, A. Muñoz, A. H. Romero, D. Errandonea, and K. Syassen, Lattice dynamics of YVO_4 at high pressures, Phys. Rev. B **81**, 075202 (2010).

[70] R. Rao, A. B. Garg, T. Sakuntala, S. N. Achary, and A. K. Tyagi, High pressure Raman scattering study on the phase stability of $LuVO_4$, J. Solid State Chem. **182**, 1879 (2009).

[71] V. Panchal, D. Errandonea, F. J. Manjón, A. Muñoz, P. Rodríguez-Hernández, S. N. Achary, and A. K. Tyagi, High-pressure lattice-dynamics of $NdVO_4$, J. Phys. Chem. Solids **100**, 126 (2017).

[72] F. J. Manjón, D. Errandonea, N. Garro, J. Pellicer-Porres, P. Rodríguez-Hernández, S. Radescu, J. López-Solano, A. Mujica, and A. Muñoz, Lattice dynamics study of scheelite tungstates under high pressure, I. $BaWO_4$, Phys. Rev. B **74**, 144111 (2006).

[73] M. Nicol and J. F. Durana, Vibrational Raman spectra of $CaMoO_4$ and $CaWO_4$ at high pressures, J. Chem. Phys. **54**, 1436 (1971).

[74] P. Botella, R. Lacomba-Perales, D. Errandonea, A. Polian, P. Rodriguez-Hernandez, and A. Munoz, High-pressure Raman scattering of $CaWO_4$ up to 46.3 GPa: Evidence of a new high-pressure phase, Inorg. Chem. **53**, 9729 (2014).

[75] A. Grzechnik, Local structures in high pressure phases of V_2O_5, Chem. Mater. **10**, 2505 (1998).

[76] V. Panchal, D. Errandonea, A. Segura, P. Rodriguez-Hernandez, A. Muñoz, S. Lopez-Moreno, and M. Bettinelli, The electronic structure of zircon-type orthovanadates: Effects of high-pressure and cation substitution, J. Appl. Phys. **110**, 043723 (2011).

[77] E. Bandiello, J. Sánchez-Martín, D. Errandonea, and M. Bettinelli, Pressure effects on the optical properties of $NdVO_4$, Crystals **9**, 237 (2019).

[78] See Supplemental Material at http://link.aps.org/supplemental/10.1103/PhysRevB.100.064106 for a brief discussion on the described optical absorption experiments as well as information about the theoretical evolution with pressure of the infrared and silent modes of zircon- and scheelite-type $GdVO_4$.

[79] F. Urbach, The long-wavelength edge of photographic sensitivity and of the electronic absorption of solids, Phys. Rev. **92**, 1324 (1953).

[80] A. H. Krumpel, E. Van der Kolk, E. Cavalli, P. Boutinaud, M. Bettinelli, and P. Dorenbos, Lanthanide $4f$-level location in AVO_4:Ln^{3+} (A= La, Gd, Lu) crystals, J. Phys.: Condens. Matter **21**, 115503 (2009).

[81] S. J. Duclos, A. Jayaraman, G. P. Espinosa, A. S. Cooper, and R. G. Maines, Raman and optical absorption studies of the pressure-induced zircon to scheelite structure transformation in $TbVO_4$ and $DyVO_4$, J. Phys. Chem. Solids **50**, 769 (1989).

[82] M. R. Dolgos, A. M. Paraskos, M. W. Stoltzfus, S. C. Yarnell, and P. M. Woodward, The electronic structures of vanadate salts: Cation substitution as a tool for band gap manipulation, J. Solid State Chem. **182**, 1964 (2009).

[83] D. Errandonea and F. J. Manjón, On the ferroelastic nature of the scheelite-to-fergusonite phase transition in orthotungstates and orthomolybdates, Mater. Res. Bull. **44**, 807 (2009).

[84] A. Malik, A. Hakeem, D. E. Jackson, J. J. Hamlin, D. Errandonea, J. E. Proctor, and M. Bettinelli, High pressure Raman, optical absorption, and resistivity study of $SrCrO_4$, Inorg. Chem. **57**, 7550 (2018).

[85] H. Nyman, B. G. Hyde, and S. Andersson, Zircon, anhydrite, scheelite and some related structures containing bisdisphenoids, Acta Cryst. B **40**, 441 (1984).

[86] M. Flórez, J. Contreras-García, J. M. Recio, and M. Marques, Quantum-mechanical calculations of zircon to scheelite transition pathways in $ZrSiO_4$, Phys. Rev. B **79**, 104101 (2009).

[87] E. Stavrou, A. Tatsi, C. Raptis, I. Efthimiopoulos, K. Syassen, A. Muñoz, P. Rodríguez-Hernández, J. López-Solano, and M. Hanfland, Effects of pressure on the structure and lattice dynamics of $TmPO_4$: Experiments and calculations, Phys. Rev. B **85**, 024117 (2012).

[88] J. F. Nye, *Physical properties of crystals, Their representation by tensors and matrices*, Oxford Science Publications (Clarendon Press, Oxford, 1985).

[89] D. C. Wallace, Thermoelastic theory of stressed crystals and higher-order elastic constants, Solid State Phys. **25**, 301 (1970).

[90] R. L. Melcher, The anomalous elastic properties of materials undergoing cooperative Jahn-Teller phase transitions, Phys. Acoust. **12**, 1 (1976).

[91] J. R. Sandercock, S. B. Palmer, R. J. Elliott, W. Hayes, S. R. P. Smith, and A. P. Young, Brillouin scattering, Ultrasonic and theoretical studies of acoustic anomalies in crystals showing Jahn-Teller phase transitions, J. Phys. C: Solid State Phys. **5**, 3126 (1972).

[92] T. Goto, A. Tamaki, and T. Fujimura, Quadrupolar response and rotational invariance of single ground state system: $HoVO_4$, J. Phys. Soc. Jpn. **55**, 1613 (1986).

[93] Y. Hirano, I. Guedes, M. Grimsditch, C. K. Loong, N. Wakabayashi, and L. A. Boatner, Brillouin-scattering study of the elastic constants of $ErVO_4$, J. Am. Ceram. Soc. **85**, 1001 (2002).

[94] M. Born and K. Huang, *Dynamical Theory of Crystal Lattices* (Oxford University Press, Oxford, 2007).

[95] D. C. Wallace, Thermoelasticity of stressed materials and comparison of various elastic constants, Phys. Rev. **162**, 776 (1967).

[96] G. Grimvall, B. Magyari-Köpe, V. Ozoliņš, and K. A. Persson, Lattice instabilities in metallic elements, Rev. Mod. Phys. **84**, 945 (2012).

[97] F. Mouhat and F. X. Coudert, Necessary and sufficient elastic stability conditions in various crystal systems, Phys. Rev. B **90**, 224104 (2014).

[98] R. Mittal, M. K. Gupta, B. Singh, L. Pintschovius, Y. D. Zavartsev, and S. L. Chaplot, Phonon dispersion relation, High-pressure phase stability and thermal expansion in YVO_4, Phys. Rev. Mater. **3**, 043608 (2019).

[99] W. Voigt, *Lehrbuch der Kristallphysik* (Teubner, Leipzig, 1928), Vol. 962.

[100] A. Reuss, Account of the liquid limit of mixed crystals on the basis of the plasticity condition for single crystal, Z. Angew. Math. Mech. **9**, 49 (1929).

[101] R. Hill, The elastic behavior of a crystalline aggregate, Proc. Phys. Soc. A **65**, 349 (1952).

[102] S. F. Pugh, Relations between the elastic moduli and the plastic properties of polycrystalline pure metals, Lond. Edinb. Dubl. Philos. Mag. J. Sci. **45**, 82 (1954).

[103] A. M. Hofmeister, IR spectroscopy of alkali halides at very high pressures: Calculation of equations of state and of the response of bulk moduli to the B1− B2 phase transition, Phys. Rev. B **56**, 5835 (1997).

[104] D. Errandonea, R. Boehler, and M. Ross, Melting of the Rare Earth Metals and *f*-Electron Delocalization, Phys. Rev. Lett. **85**, 3444 (2000).